Light-to-heat conversion and photothermal hydrogen evolution over magnetic nitinol photocatalyst

Sergey I. Nikitenko, Sara El Hakim, Xavier Le Goff, Tony Chave

Light-to-heat conversion and photothermal hydrogen evolution over magnetic nitinol photocatalyst

Sergey I. Nikitenko,* Sara El Hakim, Xavier Le Goff, Tony Chave

ICSM, Univ Montpellier, CEA, CNRS, ENSCM, Marcoule, France

E-mail address: serguei.nikitenko@cea.fr

Abstract

Development of efficient photothermal catalysts made of earth-abundant elements is of prime importance for heterogeneous photocatalysis driven by solar light. Herein, we report for the first time the synthesis of NiTi@TiO_2/Ni core-shell-satellite nanoparticles from pristine nitinol nanopowder (NiTi) by simple and easily scalable ultrasonically assisted hydrothermal treatment in pure water (T = 200 °C, P = 14 bar, f = 20 kHz, P_{ac} = 17 W, τ = 3 h). Prepared material exhibits unique set of properties, such as strong capability of light-to-heat conversion, good magnetization, high stability, and remarkable thermally assisted photocatalytic hydrogen production (5.5 $mmol \cdot h^{-1} \cdot g^{-1}$ at T = 90 °C). The core-shell-satellite morphology of NiTi@TiO_2/Ni particles maximizes the contact area between the heat generating metallic core and photocatalytically active TiO_2/Ni nanocrystalline shell providing the most efficient photothermal effect in the processes of H_2 production and CO_2 methanation without CO emission. In addition, significant magnetic susceptibility of the NiTi@TiO_2/Ni nanoparticles allows their easy recovery from solution with an external magnetic field. Noncongruent surface oxidation of nanoalloys reported in this work paves the way to the preparation of new generation of catalysts with advanced photothermal properties.

Keywords: nitinol, photothermal effect, photocatalysis, hydrogen production, methanation, H/D kinetic isotope effect

Introduction

Solar energy can be harnessed in various processes ranged from electricity production and heating to prompting chemical reactions via photocatalysis. Introducing heat into photocatalytic processes has attracted a great deal of attention in the last decade because it may significantly improve the photoconversion efficiency [1]. In addition, self-heating of the photocatalytic systems can provide a lower energy consumption to convert substrates into desired products [2]. Metallic fine particles have proven to be effective in both processes due to the broad light spectral harvesting and advanced photocatalytic activity. Photon absorption at the surface of metallic particles results in the electron-hole formation via nonradiative Landau damping mechanism [3]. However, in a highly conducting metallic material formed electron-hole pairs will recombine rapidly producing strong local heating. On the other hand, high electric conductivity implies high carrier mobility, and this might allow electron-hole separation in the presence of carrier scavengers, such as adsorbed molecular species or semiconducting metal particle supports leading to photocatalytic activity [3,4]. The efficiency of photothermal catalysts depends strongly on their composition, optical properties, particle size and morphology [2,5,6]. Plasmonic gold nanoparticles (NPs) were shown to be efficient for photothermal catalysis [7] and for solar vapor generation [8]. Large number of recent studies

was focused on photothermal solar fuel production (H_2, CO, CH_4) in aqueous solutions of sacrificial reagents and in gas phase (water-gas shift process, Sabatier reaction etc.) over noble metal NPs anchored on the semiconductor surface. Strong photothermal effect was reported for a number of plasmonic and nonplasmonic photocatalysts, such as Au/TiO_2 [9], Pt/TiO_2 [10-15], Pt/ZrO_2 [16,17], Pd/TiO_2 [18], Pd/ZrO_2 [16], RuS_2/TiO_2 [19], $RuO_2/Pt/TiO_2$ [20], $RuO_2/SrTiO_3$ [21], Rh/ZrO_2 [16]. These specific examples are not in any way exhaustive and only serve to illustrate the principal types of viable photothermal catalysts reported in the literature.

It is worth noting that the high price of noble and rare metals limits their large-scale application in photocatalysis. Therefore, the development of alternatives is strongly desired. As a non-noble earth abundant metal, nickel was extensively used in various catalytic processes [22,23]. Metallic nickel and some nickel-based compounds are known to be promising cocatalysts in photocatalytic systems with semiconducting supports due to the strong light absorption, increasing active sites, and boosting charge separation by the formation of Shottky junctions, ohmic contacts, and p-n junctions [24]. In the gas phase, Mateo et al. reported efficient photothermal conversion of CO_2 to CO and CH_4 at $H_2/CO_2 = 4$ over $Ni/BaTiO_3$ nanocatalyst [25]. It is interesting that the irradiation of this catalyst with 300 W Xe lamp caused its temperature increase up to ca. 350 °C in the absence of any other external source of heat. In aqueous solutions of sacrificial reagents, Ni and core-shell Ni@NiO NPs loaded on the semiconducting supports show high photocatalytic activity in the process of hydrogen evolution [26-31]. On the other hand, it was shown that small Ni or Ni@NiO NPs (≤10 nm) anchored on TiO_2 undergo photocorrosion in aqueous medium leading to the dissolution of metallic nickel and catalyst deactivation [32]. Encapsulation of Ni NPs with N-doped graphene prior deposition at $SrTiO_3$ ($Ni@NC/SrTiO_3$) improves their stability and photocatalytic performance as well [33].

Nickel oxides have also attracted a lot of attention as an efficient cocatalyst in the photocatalytic processes. NiO_x is a typical p-semiconductor, and the p-n heterojunctions at the interface with TiO_2 provide effective charge separation and therefore the catalysts $NiO_x(1<x<2)/TiO_2$ exhibit significant photocatalytic activity [34-36]. In addition, 2D amorphous NiO nanoflakes can act as a photocatalyst even without any cocatalysts [37]. Combination of CrO_x and Ni/NiO NPs deposited at the surface of Mg(II)-doped $SrTiO_3$ improves photocatalytic water splitting under UV light exposure [38]. Surprisingly, little research has been focused on the photothermal effects with nickel-based photocatalysts in solutions. Recently, Song et al. reported that the rate of aqueous methanol reforming in the presence of Ni_2P/TiO_2 composite is in 3.6 times larger under the joint effect of heat and light than that of the sum of the solely photocatalytic and thermocatalytic reactions [39]. Observed photothermal effect was ascribed to the thermally enhanced charge transport at the Ni_2P/TiO_2 interface. It is interesting to note that even at near room temperature Ni_2P/TiO_2 exhibits higher H_2 photocatalytic production rate compared to NiO/TiO_2, $Ni(OH)_2/TiO_2$, and NiS/TiO_2 photocatalysts [40].

The morphology of the nanocatalysts may strongly affect photothermal and photocatalytic efficiency. In particular, particles with core-shell structure have attracted significant attention due to the combination of multiple components, such as enhanced light-to-heat conversion, efficient charge separation, adjusting the catalyst structure, and high chemical stability [1, 2, 41, 42]. Regarding core-shell photocatalysts with nickel, only few of them are reported in the literature. In addition to cited above Ni@NiO and $Ni@NC/SrTiO_3$ NPs, Singh et al reported

enhanced photocatalytic activity of Ni@NiO/$NiCO_3$ NPs in the process of H_2 evolution compared to Ni@NiO NPs [43, 44]. Higher photocatalytic response has been attributed to the efficient charge transfer from $NiCO_3$ surface to the adsorbed water molecule.

In general, Ni NPs are prepared using hazardous reducing reagents (hydrazine, phosphonic acid) or reduction of Ni(II) with H_2 at high temperature hindering the scalability of nickel-based photocatalysts [25, 29, 39]. Herein, we report for the first time the synthesis, photothermal and photocatalytic behavior of the noble metal-free NiTi@TiO_2/Ni core-shell-satellite NPs obtained from the commercially available nitinol, NiTi, nanopowder by simple and easily scalable ultrasonically assisted hydrothermal treatment in pure water. Nitinol alloy is well known due to its shape-memory properties resulting from the pseudoelastic effect [45]. This material has already found various applications in biomedicine, aerospace, and instrumentation [46, 47]. However, to our knowledge, the catalytic properties of nitinol have never been reported. As will be shown below, the NiTi@TiO_2/Ni NPs exhibit unique set of properties, such as strong capability of heat generation under light irradiation, good magnetization, high stability, and remarkable thermally assisted photocatalytic activity.

Experimental section

Synthesis

The synthesis of NiTi@TiO_2/Ni particles was performed by simultaneous hydrothermal (T = 200 °C, P = 14 bar) and ultrasonic (f = 20 kHz, Pac = 17 W) treatment (SHT) of NiTi nanopowder (American Elements) in pure water (Milli-Q 18.2 MΩ cm at 25° C) for 3 h. Further experimental details and the graphical sketch of sonohydrothermal reactor are presented in the Supplementary Information (Fig. S1). The same approach was employed previously for the preparation of Ti@TiO_2 photocatalyst [48, 49].

Characterization

PXRD diagram in Fig. 1 and Rietveld refinement of the PXRD data (Table 1) show the phase composition of the pristine and SHT treated nitinol NPs. In agreement with the literature [50, 51], at near room temperature the pristine NiTi NPs are mainly composed of the cubic B2 phase (austenite) with some admixtures of the monoclinic martensitic phase and the intermetallic Ni_3Ti phase. As it has recently been reported, the Ni_3Ti can be formed during partial surface oxidation of NiTi [52]. The SHT treatment leads to the appearance of metallic Ni and anatase TiO_2 patterns indicating non-congruent oxidation of nitinol in hydrothermal water. The preferential oxidation of Ti at the surface of the bulk NiTi alloy has been explained previously by the enrichment of NiTi surface with Ti atoms and by the thermodynamic stability of Ni NPs embedded into TiO_2 matrix [52, 53].

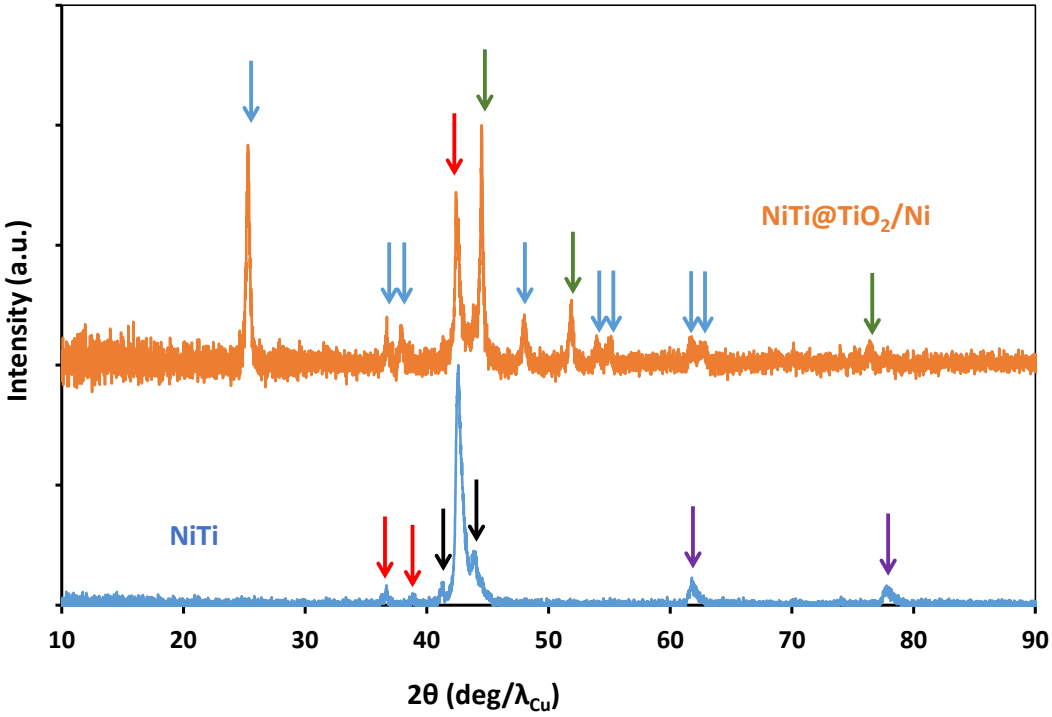

Fig. 1. PXRD patterns of pristine nitinol (NiTi) and SHT treated nitinol (NiTi@TiO_2/Ni) nanopowders. (→) NiTi cubic PDF 00-018-0899, (⟶) NiTi monoclinic PDF 00-035-1281, (⟶) Ni_3Ti PDF 00-051-1169, (⟶) Ni PDF 00-004-0850, (→) TiO_2 anatase PDF 00-064-0863.

Table 1. Phase composition of the pristine (NiTi) and SHT treated (NiTi@TiO_2/Ni) nitinol nanopowders.

Sample	mol % (±10 %)				
	NiTi cubic	NiTi monoclinic	Ni_3Ti	Ni	TiO_2
NiTi	91	5	4	–	–
NiTi@TiO_2/Ni	31	–	<1	34	35

The pristine NiTi NPs are composed of the quasi-spherical particles with an average size of around 20-100 nm without any crystals at the surface (Fig. 2a and Fig. S3). On the other hand, the STEM image of the single NiTi particle shown in Fig. 2b indicates clearly the presence of the passivating layer with the thickness about 4 nm. The complementary STEM/EDX mapping of the NiTi NPs are provided in Supplementary Information (Fig. S4). The SHT treatment leads to the formation of nanocrystalline shell composed of 15-25 nm truncated bipyramidal TiO_2 anatase particles and polyhedral Ni crystalline NPs (ca. 20 nm) as it is displayed in Fig. 3a. The specific surface area of SHT treated nitinol (S_{BET} = 10 $m^2\ g^{-1}$) was found to be larger than that of pristine nitinol (S_{BET} = 5 $m^2\ g^{-1}$), which could be attributed to the formation of nanocrystalline shell. The STEM/EDX mapping data shown in Fig. 3b and Fig. S5 reveal that the most of Ni

NPs are attached onto TiO_2 shell forming core-shell-satellite structure. We suggest that this design maximizes the contact area between the heat generating metallic core and photocatalytically active TiO_2/Ni nanocrystalline shell providing the most efficient photothermal effect. It should be noted that the catalytic properties of core-shell-satellite NPs are still poorly understood. However, very recently it was reported that the Ag@SiO_2@CdS/Au NPs exhibit largely improved photocatalytic performance compared with traditional CdS/Au NPs [54].

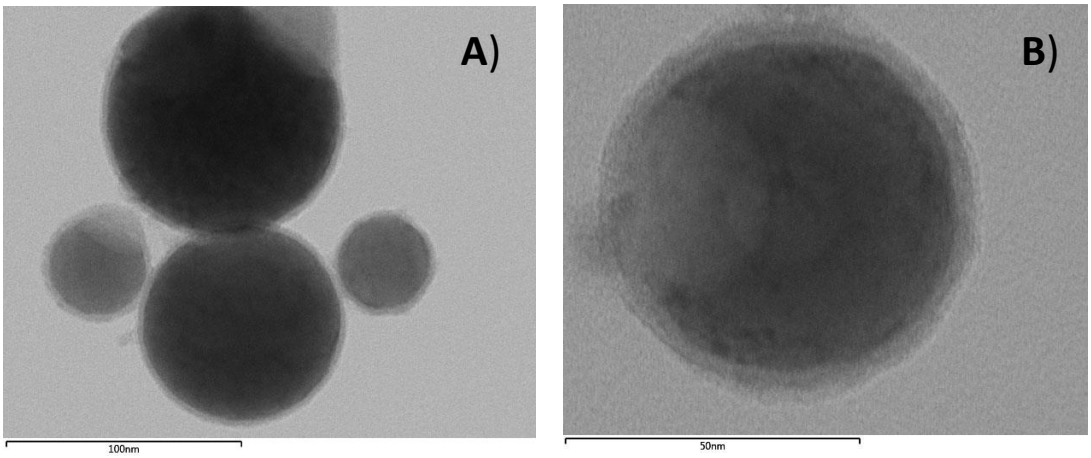

Fig. 2. STEM images of pristine NiTi particles. Corresponding STEM/EDX mapping is shown in Fig. S4.

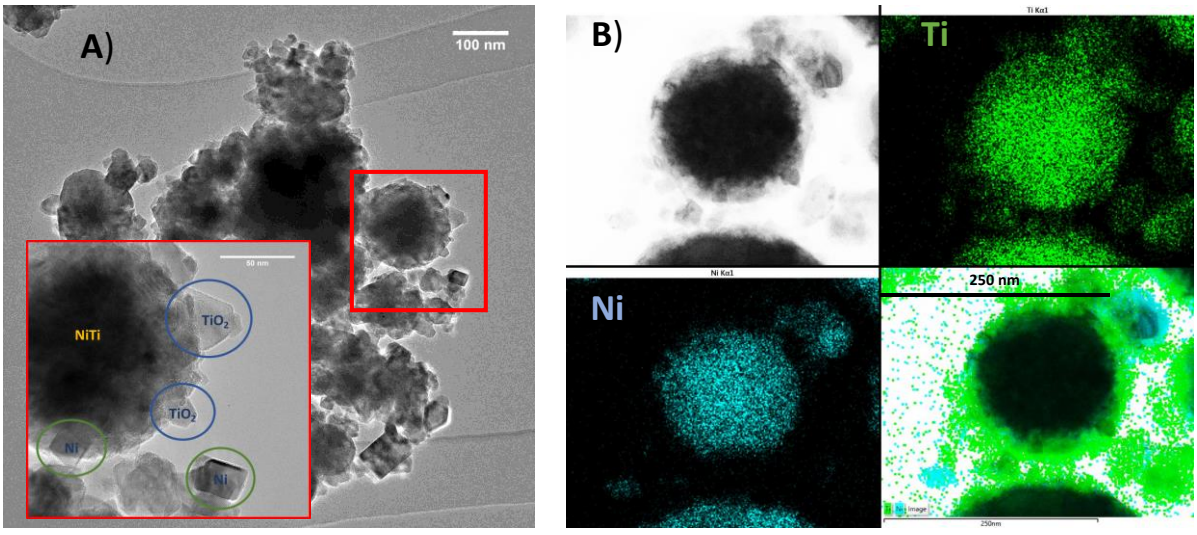

Fig. 3. HRTEM images of NiTi@TiO_2/Ni NPs obtained after SHT treatment of NiTi NPs (Fig. 3a) and ultra-microtomographic image of core-shell-satellite NiTi@TiO_2/Ni particle coupled with EDX mapping of Ni (blue) and Ti (green) (Fig. 3b).

The surface chemical composition of NiTi and NiTi@TiO_2/Ni NPs was studied by XPS. Table 2 summarizes the results of high-resolution XPS for O 1s, Ti 2p and Ni 2p states. The corresponding spectra are shown in Supplementary Information (Fig. S6-S7). The spectra were fitted using binding energies (BE) published in the NIST database [55]. The XPS profiles of O 1s envelop for both samples indicate the presence of several oxygen species, which can be assigned to the chemisorbed water molecules, surface hydroxide groups and lattice oxygen of the oxidized Ti and Ni compounds at the surface of NPs. The Ti 2p envelop of NiTi NPs is dominated by TiO_2 signal with some small amounts of Ti^0 and lower oxidation states of titanium (TiO, Ti_xO_y Ti_2O_3). The Ni 2p spectrum is characterized by the intense signal of Ni^{2+} at 855.4 eV and a satellite peak at 861.2 eV typical for NiO [56]. In addition, peak at 852.0 eV indicates the presence of metallic nickel. It should be noted that, in contrast to XPS, titanium and nickel oxidized species are not observed by PXRD of pristine NiTi, which can be attributed to their amorphous state or low concentration in bulk material. The peaks of Ti^0 and low oxidation states of titanium have disappeared after SHT treatment. On the other hand, the XPS spectra exhibit the patterns of TiO_2 and partially oxidized Ni^0 in an agreement with core-shell-satellite morphology of NiTi@TiO_2/Ni NPs. In general, the XPS data show clearly the enrichment of NiTi NPs surface with titanium species in agreement with recently published data for the bulk NiTi alloy [52, 53].

Table 2. XPS analysis of pristine (NiTi) and SHT treated (NiTi@TiO_2/Ni) nitinol NPs.

Species	BE (eV)	Atomic % (±5 %)	
		NiTi	NiTi @TiO_2/Ni
O 1s A	529.76	38.0	36.1
O 1s B	531.08	18.0	15.6
O 1s C	532.21	7.7	12.4
O 1s D	533.34	3.6	4.0
Ti^0 2p	454.01	1.2	0
TiO 2p	455.15	0.8	0
Ti_xO_y 2p	456.23	1.0	0
Ti_2O_3 2p	457.21	0.7	0
TiO_2 2p	458.35	21.8	17.5
Ni^0 2p	852.0	2.5	3.2
NiO 2p	861.20	5.6	11.2

We found that NiTi@TiO_2/Ni NPs exhibit distinct magnetic properties. Fig. 4 depicts the plot of magnetization vs external magnetic field for NiTi and NiTi@TiO_2/Ni NPs. The pristine NiTi NPs show very low magnetization. According to the literature, the origin of NiTi magnetic susceptibility is expected to be of Pauli paramagnetism [57]. By contrast, magnetization curve of NiTi@TiO_2/Ni NPs reveals its ferromagnetic behavior. The magnetic properties of NiTi@TiO_2/Ni NPs are most likely related to the presence of magnetic Ni^0 NPs in the shell of obtained material. It is known that the saturation magnetization, M_S, of Ni^0 NPs is strongly dependent on their shape and size and varies in the range of 23 – 48 emu g^{-1} at room temperature [58, 59]. The M_S value of NiTi@TiO_2/Ni NPs normalized to the amount of Ni^0 calculated using XRD data (Table 1) is equal to M_S =

38 emu g^{-1} in line with the published data. The significant magnetic susceptibility enables NiTi@TiO_2/Ni NPs recovery from aqueous suspensions with an external magnetic field as it is shown in the inset of Fig. 4. These data clearly indicate that magnetic Ni^0 NPs are associated with non-magnetic NiTi@TiO_2 core.

Both materials, NiTi and NiTi@TiO_2/Ni, have intense black color indicating effective solar light harvesting. As shown in Fig. 5, the absorption spectrum of pristine NiTi exhibits a broad continuum spanning from UV to NIR spectral range typical for interband/intraband transitions in non-plasmonic metals [60]. On the other hand, several clearly distinguishable absorption bands are observed in the spectrum of NiTi@TiO_2/Ni NPs in addition to broad continuum. The broad band at 250-350 nm centered at ca. 320 nm is ascribed to the bandgap of TiO_2 similar as previously reported for Ti@TiO_2 NPs [49]. The peak at ca. 270 nm and barely visible broad adsorption band centered at ca. 770 nm are attributed to localized surface plasmon resonance (LSRP) of Ni^0 and far-field (FF) optical response of the magnetoplasmonic rulers respectively [61, 62]. The FF absorption band is triggered by dipole-dipole interactions of Ni^0 NPs. When two metallic NPs that individually show a LSRP are placed close to one another, additional forces act upon the polarization of both particles, splitting the original plasmon modes. Consequently, the relative intensity of the FF band strongly depends on the interparticle distance. Therefore, the low intensity of the FF band could be explained by Ni^0 NPs separation with TiO_2 NPs in the core-shell-satellite structure.

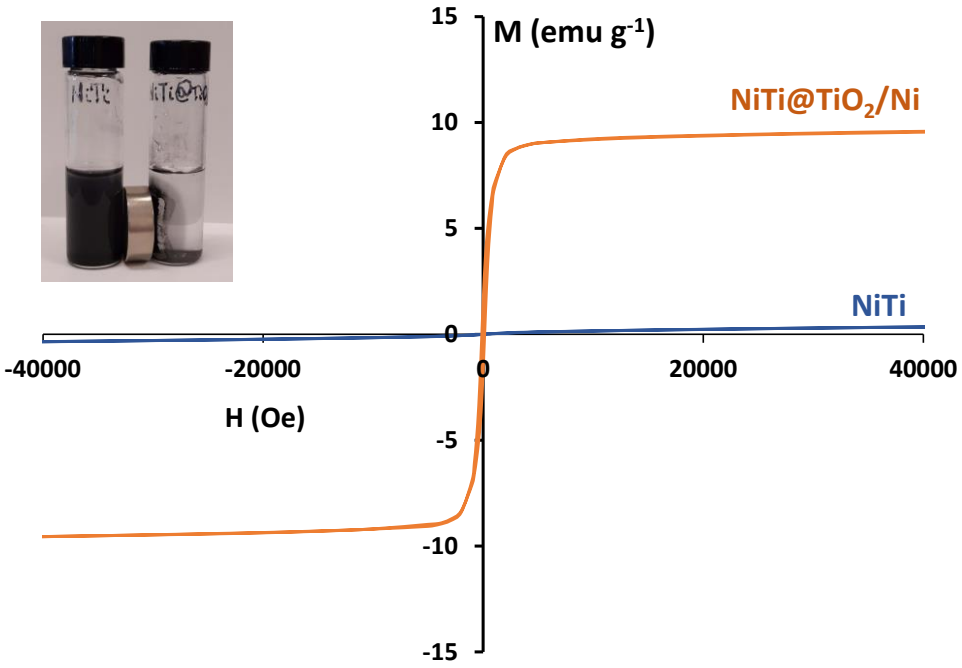

Fig. 4. Magnetization curves for NiTi and NiTi@TiO_2/Ni NPs measured at room temperature. The inset shows magnetic response of NiTi (left) and NiTi@TiO_2/Ni (right) in aqueous suspensions. Permanent magnet is in the middle.

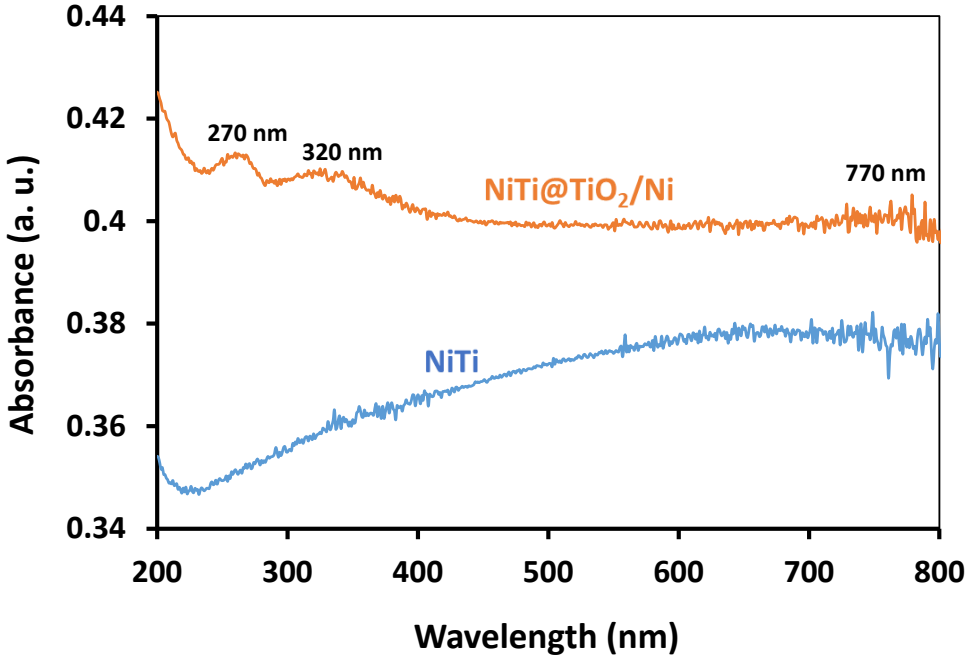

Fig. 5. UV/vis/NIR absorption spectra of NiTi and NiTi@TiO_2/Ni NPs suspended in water using ultrasonic bath dispersion. Concentration of solids is 100 ppm. Optical length is 1 cm. Comparison of the optical spectra for nitinol and pristine TiO_2 is shown in Supplementary Information (Fig. S8).

Results and discussion

Light-to-heat conversion

The photothermal experiments were performed in aqueous suspensions of NiTi and NiTi@TiO_2/Ni NPs under the irradiation with a white light of xenon lamp. Further details about the photothermal experiments are presented in Supplementary Information (Fig. S2). The concentration of NPs in suspensions was 100 mg L^{-1}. In the preliminary experiments, it was found that more than 95% of the incident light is absorbed at this concentration. Fig. 6 shows that during illumination the bulk temperature of colloidal suspensions is gradually increased reaching a steady-state value around 75 °C. The heating curves for NiTi and NiTi@TiO_2/Ni NPs are very similar indicating that the self-heating effect is determined by NiTi metallic core rather than by TiO_2/Ni shell. In general, metal NPs exhibit strong photothermal properties because they have high free electron density [7,8]. For a given light intensity, the maximum temperature increase provided by metallic particles, ΔT_{max}, is determined by two factors: (i) the total heat generation rate proportional to the particle volume; and (ii) the total heat current from the particle surface proportional to the particle surface area [63]. Hence, the temperature increase is roughly proportional to the second power of the particle radius:

$$\Delta T_{max} \approx R_{NPs}^2 \qquad (1)$$

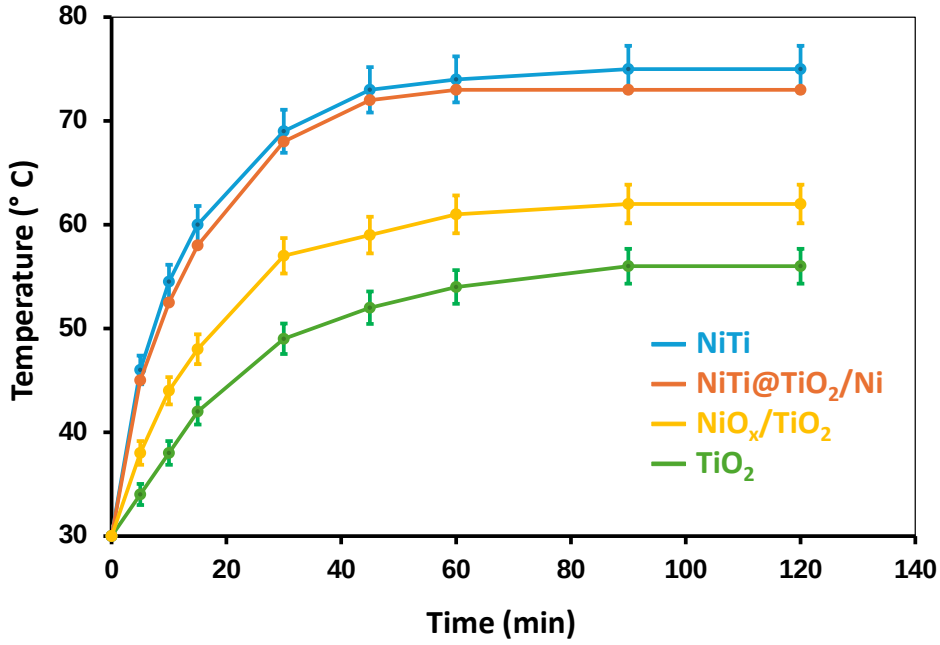

Fig. 6. Temperature evolution with time under Xe lamp exposure for the aqueous suspensions of NiTi, NiTi@TiO_2/Ni, NiO_x/TiO_2, and TiO_2 anatase NPs. Concentration of NPs is 100 mg L^{-1}. The absorbed light power is 8.9 W and 0.6 W for vis/NIR and UV spectral ranges respectively. The optical length of the cell is 3.5 cm. Water jacket of the cell is empty to reduce thermal losses. The temperature measurement uncertainty for NiTi@TiO_2/Ni is the same as for NiTi.

It can therefore be concluded that the strongest self-heating effect is produced by largest NPs with the size of ca. 100 nm (Fig. 2, 3). For comparison, Fig. 6 also demonstrates the heating curves for NiO_x/TiO_2 NPs, which is frequently reported as noble metal-free efficient photocatalyst, and commercial anatase TiO_2 NPs (d ≈ 20 nm) aqueous suspensions. The NiO_x/TiO_2 catalyst was prepared by conventional impregnation method reported in the literature [34,35]. Detailed description of the catalyst synthesis is presented in Supplementary Information. Fig. 6 shows clearly much lower heat generation efficiency of the pristine TiO_2 and NiO_x/TiO_2 NPs compared to that of NiTi and NiTi@TiO_2/Ni NPs. In contrast to metallic NPs, the self-heating of semiconducting particles, such as TiO_2 and NiO_x/TiO_2, is ascribed to the recombination of photogenerated electron-hole pairs [2,3]. In the pristine TiO_2, photoexcitation occurs mostly by UV part of light produced by Xe lamp (c.a. 6% of the full spectrum). Therefore, this material exhibits relatively low light to heat conversion efficiency. It is noteworthy that the photothermal effect of NiO_x/TiO_2 is somewhat larger compared to TiO_2 due to the better visible light harvesting of nickel oxide loaded titania [34,35].

Photothermal catalysis

The photocatalytic activity of NiTi and NiTi@TiO_2/Ni NPs and conventional TiO_2 anatase NPs was explored in aqueous solutions of 1M glycerol using a thermostated gas-flow cell (Fig. S2) adapted to mass spectrometric analysis of the outlet gases. The details of the mass spectrometric analysis are described in Supplementary Information. The two thermal regimes were included in this study: (i) self-heating when only the white light of the Xe lamp was used as a source of heat without any external temperature control and (ii) assisted heating when the temperature inside the photocell during light exposure was controlled with a thermostat.

Self-heating

Online mass spectrometric analysis of the outlet carrier gas revealed the photocatalytic formation of predominantly H_2 and CH_4, accompanied by lesser amounts of CO_2. Fig. 7 and Fig. S9 show that upon light exposure the concentration of photocatalytic products in the outlet gas gradually increases with temperature rise reaching a steady state value simultaneously with that of temperature. On the other hand, the heating at 75 °C under dark conditions does not lead to gaseous products formation indicating the photonic origin of the process. It is worth noting that the amount of formed CO was below the detection limit of the mass spectrometer (0.5 ppm) for all studied systems. It is interesting that the photothermal methanol reforming over NiO_x/TiO_2 catalyst yields H_2 and CO as principal products without CH_4 [64] suggesting a significant difference of the reaction mechanism compared to nitinol-based catalyst.

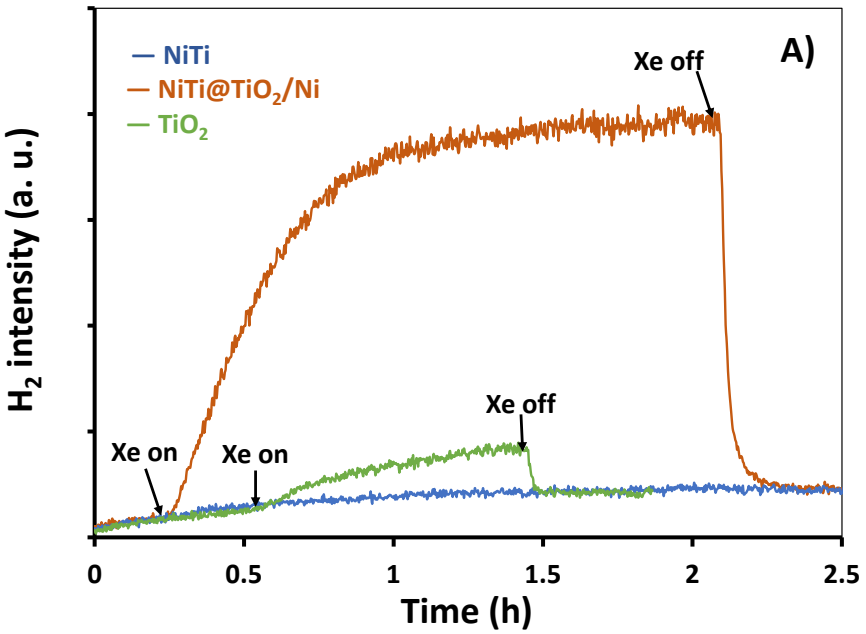

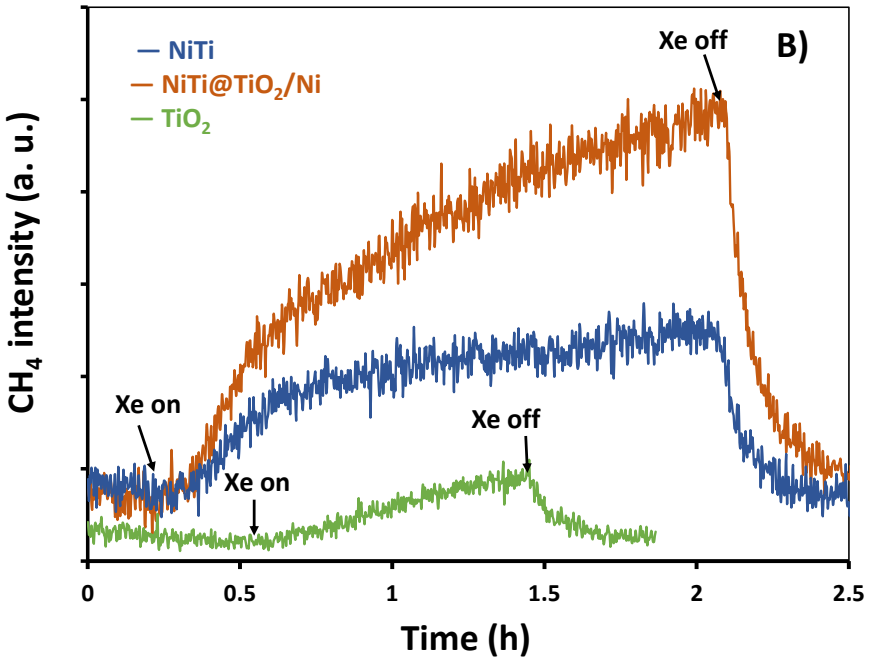

Fig. 7. Emission profiles of H_2 and CH_4 under Xe lamp exposure for the suspensions of 100 ppm of NiTi, NiTi@TiO_2/Ni, and TiO_2 anatase NPs in 1M glycerol at the self-heating regime at 75 °C. The corresponding emission profiles of CO_2 are shown in Fig. S9.

Fig. 8 summarizes the values of reactions rates for the gaseous photocatalytic products at the steady state reached during self-heating thermal regime. The largest reaction rates of H_2, CH_4 and CO_2 production are observed over core-shell-satellite NiTi@TiO_2/Ni NPs and their values follow the order of $[H_2] >> [CH_4] > [CO_2]$. A similar kinetic behavior has been recently reported for the photocatalytic reforming of glycerol over Pt/TiO_2-Nb_2O_5 catalyst [65]. Photocatalytic H_2 evolution over NiO_x/TiO_2 NPs shown for comparison is larger than for pristine TiO_2 in agreement with previous reports [34,35]. On the other hand, its photocatalytic performance is significantly lower than that of NiTi@TiO_2/Ni NPs indicating crucial role of metallic Ni for efficient photothermal glycerol reforming.

Surprisingly, the pristine NiTi NPs also show distinct photocatalytic activity. Despite very low H_2 formation rate, the formation rate of CH_4 over NiTi is only 1.4 times smaller than over NiTi@TiO_2/Ni. In addition, CO_2 formation rate with metallic NiTi NPs is close to that of semiconducting NiO_x/TiO_2 and TiO_2 NPs indicating high selectivity of this catalyst toward CH_4 formation. Recently, it was shown that Ti^0 NPs are inert in the photocatalytic glycerol reforming [49]. Therefore, the activity of NiTi alloy most likely is attributed to the presence of metallic nickel at the surface of NPs, which have been recognized as a promising catalyst for glycerol steam-reforming [66, 67]. As mentioned above, direct photocatalysis with unsupported metallic NPs is ascribed to the nonradiative Landau damping mechanism. Therefore, the first step of glycerol photocatalytic degradation would be triggered by electron hole scavenging at the surface of photoexcited NiTi NPs. However, the efficiency of this process is relatively low because of the extremely rapid electron-hole recombination in metals. On the other hand, high

photocatalytic performance of NiTi@TiO_2/Ni NPs might be attributed to the efficient charge separation via electron trapping within satellite Ni^0 NPs and electron hole accumulation within semiconducting TiO_2 shell. It should be emphasized that not much is known about the mechanism of CH_4 formation during photocatalytic reforming of glycerol in solutions. By similarity with thermo-catalytic CH_4 production from glycerol over nickel-based catalysts in vapor- phase at ca. 400 °C [66, 67], one can suggest that CH_4 is formed by methanation of CO_2 formed during glycerol degradation. Study of glycerol photothermal reforming over NiTi@TiO_2/Ni NPs under assisted heating provided further insights onto reaction mechanism.

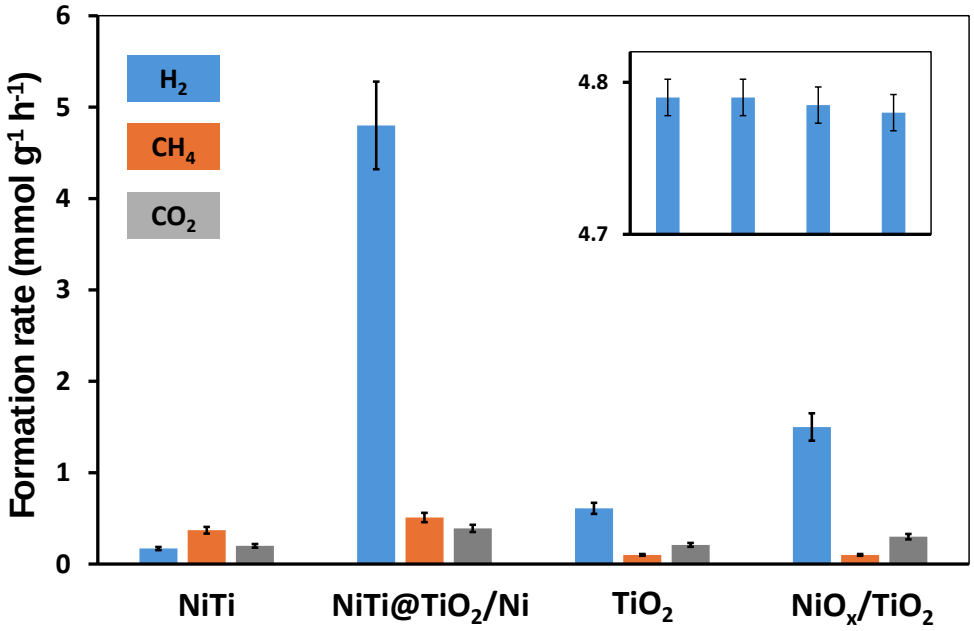

Fig. 8. Formation rates of H_2, CH_4, and CO_2 at the self-heating steady-state during Xe lamp exposure (75 °C) for the suspensions of NiTi, NiTi@TiO_2/Ni, NiO_x/TiO_2, and TiO_2 anatase NPs in 1M glycerol aqueous solution. Inset demonstrates stability test of magnetic nitinol during H_2 production for 4 cycles 4 h of light exposure each at self-heating.

Catalyst stability

The stability is one of the most important indicators for evaluating the performance of a photocatalyst. In this work, stability of NiTi@TiO_2/Ni activity in H_2 production was tested during 4 cycles of self-heating. After each 4 h cycle, the catalyst was removed with external magnet and reused with a fresh 1M glycerol solution. Slight decrease (< 5%) of H_2 production rate at the last cycle (Inset of Fig. 8) most likely is assigned to some loss of catalyst during removal rather than to its passivation. In addition, any modification of the NPs morphology has been detected by STEM analysis after these experiments, indicating high stability of magnetic nitinol in the photothermal process (Fig. S10).

Assisted heating

Surprisingly, Fig. 9 depicts ridge-shaped profiles of H_2 and CH_4 emission during photothermal glycerol reforming over NiTi@TiO_2/Ni NPs under assisted heating provided by external

thermostat in addition to self-heating with Xe lamp. A corresponding plot of CO_2 emission is shown in Fig. S11 of Supplementary information. At the bulk temperature of T > 36 °C each stepwise heating leads to a sharp jumping of the gaseous products concentration at the initial stage. Then, their concentration is dropped until some steady-state value. At 75 °C the steady-state concentration values are similar to those obtained during self-heating. Such striking behavior can be understood considering two observations: (i) at T < 36 °C the CH_4 is barely detectable and the peak value of H_2 is not observed, and (ii) the appearance of the CH_4 peak is temporally mismatched on ca. 5 min compared to that of H_2 as it can be seen from the inset of Fig. 9. Both phenomena allow to conclude that a ridge-shaped profile of gaseous products is attributed to CO_2 methanation with H_2 formed at the first stage of photothermal glycerol reforming. It should be noted that the apparent activation energy, E_a, in studied system for H_2 and CO_2 formation is much lower than for CH_4 (Table 3). Therefore, rapid external heating leads to more rapid production of H_2 and CO_2 compared to steady state. Then, kinetically less favorable methanation process would lead to the consumption of H_2 and CO_2 and drop of their concentrations until steady state values. The self-heating rate with NiTi@TiO_2/Ni NPs (3 °C min^{-1}, Fig. 6) is significantly lower than the rate of assisted heating (7 °C min^{-1} at T > 36 °C, Fig. 9). As a result, under self-heating the photocatalytic system has enough time to reach a steady-state between H_2 production and CO_2 methanation.

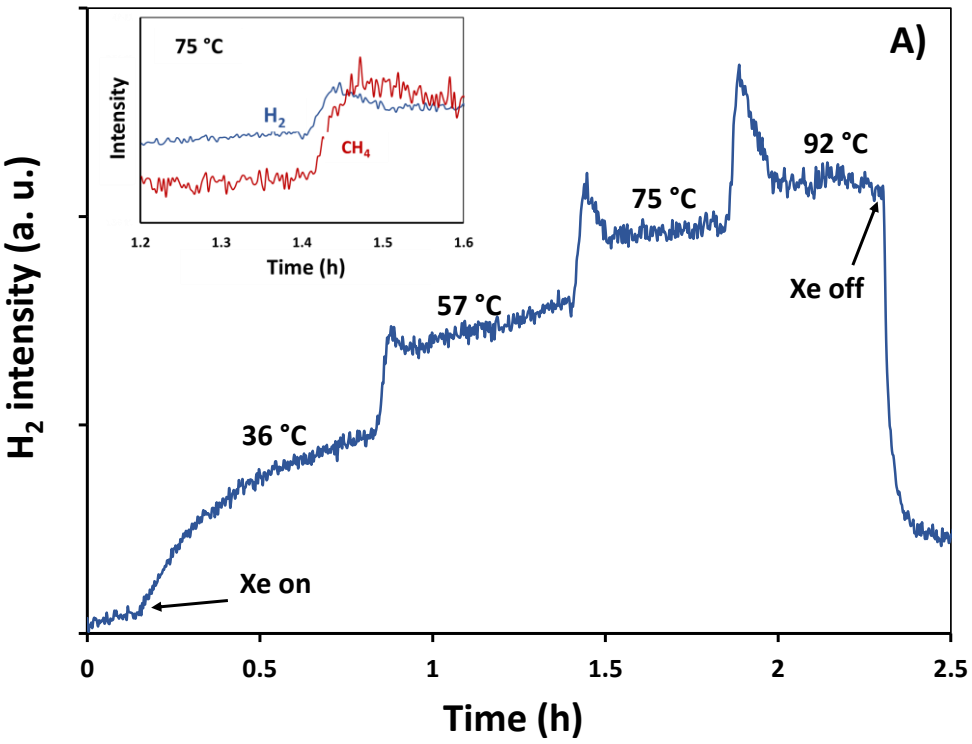

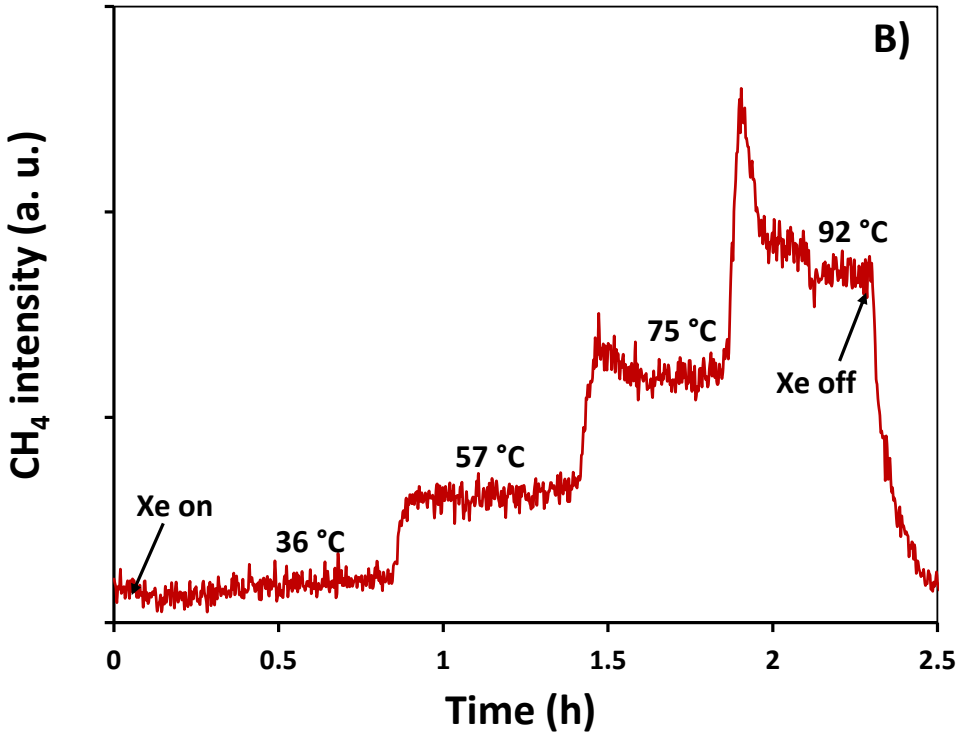

Fig. 9. Emission profiles of H_2 (A) and CH_4 (B) under Xe lamp exposure for the suspensions of 100 ppm of NiTi@TiO_2/Ni in 1M glycerol at the assisted heating regime. The corresponding emission profile of CO_2 is shown in Fig. S10. Inset shows zoom of H_2 and CH_4 peaks at 75 °C. CH_4 intensity was normalized to H_2 for comparison.

Table 3. Apparent activation energies, E_a, for H_2, CO_2, and CH_4 formation during photothermal glycerol reforming over NiTi@TiO_2/Ni photocatalyst. The E_a values were calculated from the Arrhenius plots formation rate values of for each temperature summarized in Table S1.

Product	E_a, kJ mol^{-1}
H_2	19±2
CO_2	16±2
CH_4	59±6

H/D kinetic isotope effect

To gain further information on the mechanism of photothermal process in studied system we employed the H/D kinetic isotope effect (KIE). The KIE is known to be a powerful tool to reveal the dominating reaction pathways of photocatalytic processes [68-70]. In this work, the photo-reforming of 1M glycerol was studied in 50 mol% H_2O/50 mol% D_2O mixtures over NiTi@TiO_2/Ni NPs at 92 °C. In the equimolar H_2O/D_2O mixture, water mainly presents as HDO molecules because of fast equilibrium [71]:

$$H_2O + D_2O \rightleftarrows 2HDO,\ K_{eq} = 3.4\ (T = 25\ °C) \qquad (2)$$

Mass spectrometric measurements shown that hydrogen released during photolysis in HDO solutions is composed of three isotopologues: H_2, HD, and D_2. We found that the substitution of H_2O with HDO reduces total hydrogen formation rate calculated as $R(\Sigma H_2) = R(H_2) + R(HD) + R(D_2)$ by a factor of 2.7. It is worth noting that the difference in the physicochemical properties of H_2O and HDO (strength of the hydrogen bonds, diffusion coefficient, conductivity etc.) does not exceed 5%. Therefore, the observed H/D KIE cannot be ascribed to the solvent isotope effect but to the primary KIE referred to the electron hole mediated cleavage of OH/OD bonds in the same way that it has been reported for the photocatalytic hydrogen production over Pt/TiO_2 [68], Au/TiO_2 [69], and $Ti@TiO_2$ [70] catalysts.

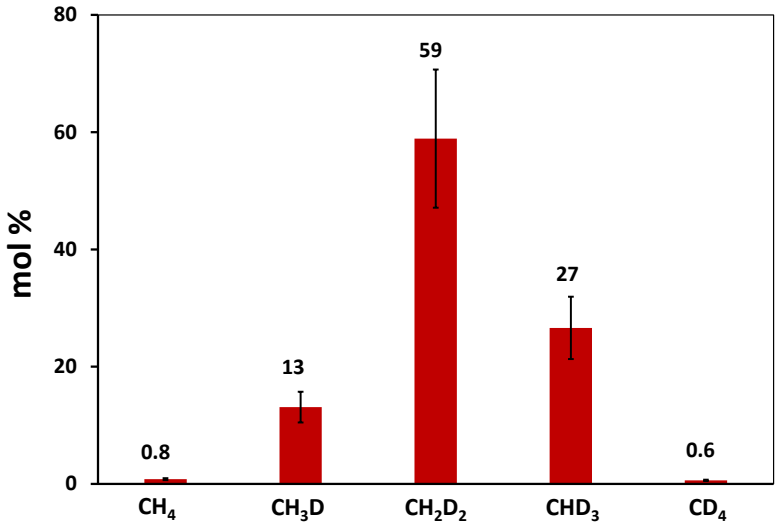

Fig. 10. Distribution of the isotopic forms of methane formed upon Xe lamp exposure of 100 ppm suspension of $NiTi@TiO_2/Ni$ NPs in 1M glycerol solution in HDO at 92 °C.

In addition, we found that formed methane is comprised of five isotopically different species CH_xD_y, where x + y =4 and y vary from 0 to 4. Fig. 10 indicates the domination of CH_2D_2 species in the isotopic mixture, which gives H/D ratio in released methane close to that of HDO. This result strongly supports the assumption that CH_4 in studied system is formed by the light-driven methanation of CO_2 with H_2. In other words, the mechanism of CO_2 photothermal conversion into CH_4 with H_2 in aqueous solutions of glycerol is quite similar to what is observed for the photothermally-induced Sabatier reaction over Ni-based photocatalysts in the gas phase [25, 72, 73]. Most likely, CH_4 formation over pristine NiTi NPs is related to the similar mechanism. However, this catalyst is less effective in the process of H_2 formation and almost all produced H_2 is consumed during CO_2 methanation stage. Finally, the mechanism of photothermal glycerol reforming over $NiTi@TiO_2/Ni$ NPs can be represented by two consecutive stages:

First stage

RCH_2OH adsorption:

$$NiTi@TiO_2/Ni + RCH_2OH \rightleftarrows [NiTi@TiO_2/Ni]\cdot RCH_2OH \quad (3)$$

Photoexcitation:

$$[NiTi@TiO_2/Ni]\cdot RCH_2OH + h\nu \rightarrow [NiTi@TiO_2{}^{h+}/Ni^{e}]\cdot RCH_2OH \quad (4)$$

RCH_2OH splitting:

$$RCH_2OH + 2h^+ \rightarrow RCHO + 2H^+ \ (\mathbf{R_1}) \quad (5)$$

$$2H^+ + 2e^- \rightarrow H_2 \quad (6)$$

$$RCHO + H_2O \rightarrow RCH(OH)_2 \quad (7)$$

$$RCH(OH)_2 + 2h^+ \rightarrow RH + CO_2 + 2H^+ \quad (8)$$

$$2H^+ + 2e^- \rightarrow H_2 \quad (9)$$

Second stage

CO_2 photocatalytic methanation:

$$CO_2 + 4H_2 \xrightarrow{hv,\ NiTi@TiO_2/Ni} CH_4 + 2H_2O \ (\mathbf{R_2}) \quad (10)$$

where RCH_2OH and RH symbolize glycerol molecule and nonvolatile products of glycerol reforming respectively. The rate of electron hole-mediated OH bond splitting $\mathbf{R_1}$ leading to H_2 emission is larger than the rate of photocatalytic CO_2 methanation $\mathbf{R_2}$ at the studied temperatures.

Conclusions

In summary, we report for the first time advanced photothermal and photocatalytic activities of $NiTi@TiO_2/Ni$ NPs. The $NiTi@TiO_2/Ni$ core-shell-satellite NPs were prepared by sonohydrothermal treatment of commercially available NiTi NPs in pure water. This synthetic approach is easily scalable and environmentally friendly. The prepared NPs are composed of 20-100 nm NiTi metallic core, nanocrystalline shell of 10-25 nm truncated bipyramidal TiO_2 anatase particles, and polyhedral Ni crystalline NPs attached to the TiO_2 shell. The optical spectrum of $NiTi@TiO_2/Ni$ NPs exhibits a broad continuum spanning from UV to NIR spectral range typical for interband/intraband transitions in metals, the bandgap of TiO_2, and localized surface plasmon resonance of Ni^0 NPs centered on ca. 270 nm. In addition, in contrast to the pristine NiTi NPs, the $NiTi@TiO_2/Ni$ NPs exhibit distinct ferromagnetic properties ascribed to the presence of Ni^0 NPs. Magnetic behavior allows easy recovery of the $NiTi@TiO_2/Ni$ NPs from solution with an external magnetic field. Both kinds of NPs, NiTi and $NiTi@TiO_2/Ni$, show excellent heat generation capacity under light exposure. Illumination of 100 ppm aqueous suspensions of these materials with xenon lamp leads to the temperature rising up to 75 °C at studied conditions without any other source of heat making them very promising for the photothermal applications. Indeed, self-heating of the glycerol solutions with $NiTi@TiO_2/Ni$ NPs promotes efficient photocatalytic reforming accompanied by the release of CO-free H_2 and CH_4 with only small amounts of CO_2. It is worth noting that even the pristine NiTi NPs exhibit distinctive thermally assisted catalytic properties, however, their catalytic performance is much less than that of $NiTi@TiO_2/Ni$ NPs. Comparative kinetic study of the thermally assisted photocatalytic glycerol reforming performed in self-heating and assisted heating regimes and H/D KIE provided new insights onto the mechanism of hydrogen emission and CO_2

methanation in studied system. Electron hole mediated OH bond cleavage is strongly involved in the limiting stage of H_2 production. This process is accompanied by the release of small amounts of CO_2. Then, the photocatalytic methanation of CO_2 with formed H_2 occurs at the active sites of the catalysts. The methanation process requires higher activation energy compared to H_2 production. In general, non-congruent surface oxidation of nano-nitinol in mild conditions reported in this work paves the way for the preparation of efficient photothermal catalysts from wide variety of nanosized alloys.

Declaration of competing interest

The authors declare that they have no known competing financial interests or personal relationships that could have appeared to influence the work reported in this paper.

Data Availability

No data was used for the research described in the article.

Acknowledgments

The authors gratefully acknowledge Dr. Valérie Flaud for XPS analysis and Dr. Corine Reibel for magnetic measurements.

Appendix A. Supporting data

Supplementary data to this article can be found online at

References

[1] Mateo D., Cerrillo J. L., Durini S., Gascon J. Fundamentals and applications of photo-thermal catalysis. Chem Soc Rev 2021; 50: 2173-2210, doi: 10.1039/D0CS00357C.

[2] Zhu L., Gao M., Peh C. K. N., G. W. Ho G. W. Solar-driven photothermal nanostructured materials designs and prerequisites for evaporation and catalysis applications. Mater Horiz 2018; 5: 323-343, doi: 10.1039/C7MH01064H.

[3] Kale M. J., Avanesian T., Christopher P. Direct photocatalysis by plasmonic nanostructures. ACS Catal 2014; 4: 116-128, doi: 10.1021/cs400993w.

[4] Aslam U., Rao V. G., Chavez S., Linic S. Catalytic conversion of solar to chemical energy on plasmonic metal nanostructures. Nature Catal 2018; 1: 656-665, doi: 10.1038/s41929-018-0138-x.

[5] Luo S., Ren X., Lin H., Song H., Ye J. Plasmonic photothermal catalysis for solar-to-fuel conversion: current status and prospects. Chem Sci 2021; 12: 5701-5719, doi: 10.1039/D1SC00064K.

[6] Ghoussoub M., Xia M., Duchesne P. N., Segal D., Ozin G. Principles of photothermal gas-phase heterogeneous CO_2 catalysis. Energy Environ Sci 2019; 12: 1122-1142, doi: 10.1039/C8EE02790K.

[7] Adleman J. R., Boyd D. A., Goodwin D. G., Psaltis D. Heterogeneous catalysis mediated by plasmon heating. Nano Lett 2009; 9: 4417-4423, doi: 10.1021/nl902711n.

[8] Neumann O., Urban A. S., Day J., Lai S., Nordlander P., Halas N. J. Solar vapor generation enabled by nanoparticles. ACS Nano 2013; 7: 42-49, doi: 10.1021/nn304948h.

[9] Nishijima Y., Ueno K., Kotake Y., Mirakoshi K., Inoue H., Misawa H. Near-infrared plasmon-assisted water oxidation. Phys Chem Lett 2012; 3: 1248-1252, doi: 10.1021/jz3003316.

[10] Han B., Hu Y. H. Highly efficient temperature-induced visible light photocatalytic hydrogen production from water. J Phys Chem C 2015; 119: 18927-18934, doi: 10.1021/acs.jpcc.5b04894.

[11] Song R., Luo B., Liu M., Geng J., Jing D., Liu H. Synergetic coupling of photo and thermal energy for efficient hydrogen production by formic acid reforming. AIChE 2017; 63: 2916-2925, doi: 10.1002/aic.15663.

[12] Velázquez J. J., Fernández-González R., Díaz L., Melián E. P., Rodríguez V. D., Núñez P. Effect of reaction temperature and sacrificial agent on the photocatalytic H_2-production of Pt-TiO_2. J Alloys Compd 2017; 721: 405-410, doi: 10.1016/j.jallcom.2017.05.314.

[13] Huaxu L., Fuqiang W., Ziming C., Shengpeng H., Bing X., Xiangtao G., et al. Analyzing the effects of reaction temperature on photo-thermo chemical synergetic catalytic water splitting under full-spectrum solar irradiation: an experimental and thermodynamic investigation. Int J Hydrog Energy 2017; 42 : 12133-12142, doi: 10.1016/j.ijhydene.2017.03.194.

[14] Kim G., Choi H. J., Kim H., Kim J., Monllor-Satosa D., Kim M., et al. Temperature-boosted photocatalytic H_2 production and charge transfer kinetics on TiO_2 under UV and visible light. Photochem Photobiol Sci 2016; 15: 1247-1253, doi: 10.1039/C6PP00263C.

[15] Zhou Y., Doronkin D. E., Zhao Z., Plessow P. N., Jelic J., Detlefs B., et al. Photothermal catalysis over nonplasmonic Pt/TiO_2 studied by operando HERFD-XANES, resonant XES, and DRIFTS. ACS Catal 2018; 8: 11398-11406, doi: 10.1021/acscatal.8b03724.

[16] Sarina S., Zhu H.-Y., Xiao Q., Jaatinen E., Jia J., Huang Y., et al. Viable photocatalysts under solar-spectrum irradiation: nonplasmonic metal nanoparticles. Angew Chem Int Ed 2014; 53: 2935-2940, doi: 10.1002/anie.201308145.

[17] Jiang C., Wang H., Lin S., Ma F., Wang Y., Ji H. Low-temperature photothermal catalytic oxidation of toluene on a core/shell SiO_2@Pt@ZrO_2 nanostructure. Ind Eng Chem Res 2019; 58: 16450-16458, doi: 10.1021/acs.iecr.9b02850.

[18] Chen Y.-W., Hsu Y.-H. Effects of reaction temperature on the photocatalytic activity of TiO_2 with Pd and Cu cocatalysts. Catalysts 2021; 11: 966, doi: 10.3390/catal11080966.

[19] Maheu C., Puzenat E., Afanasiev P., Cardenas L., Geantet C. Photocatalytic production of H_2 is a multi-criteria optimization problem: case study of RuS_2/TiO_2. Catal Today 2021; 377: 166-175, doi: 10.1016/j.cattod.2020.07.041.

[20] Li B., Ding Y., Li Q., Guan Z., Zhang M., Yang J. The photothermal effect enhance visible light-driven hydrogen evolution using urchin-like hollow RuO_2/Pt/TiO_2/C nanomaterial. J Alloys Compd 2021; 890: 161722, doi: 10.1016/j.jallcom.2021.161722.

[21] Mateo D., Albero J., Garcia H. Titanium-perovskite-supported RuO_2 nanoparticles for photocatalytic CO_2 methanation. Joule 2019; 3: 1949-1962, doi: 10.1016/j.joule.2019.06.001.

[22] Chirik P. J. Catalysis without precious metals, Wiley-VCH Verlag GmbH & Co. KGaA 2010; 83–110.

[23] Yusuf M., Farooqi A. S., Keong L. K., Hellgardt K., Abdullah B. Contemporary trends in composite Ni-based catalysts for CO_2 reforming of methane. Chem Eng Sci 2021; 229: 116072, doi: 10.1016/j.ces.2020.116072.

[24] Wang Z., Fan J., Cheng B., Yu J., Xu J. Nickel-based cocatalysts for photocatalysis: hydrogen evolution, overall water splitting and CO_2 reduction. Mater Today Phys 2020; 15: 100279, doi: 10.1016/j.mtphys.2020.100279.

[25] Mateo D., Morlanes N., Maity P., Shterk G., Mohammed O. M., Gascon J. Efficient visible-light driven photothermal conversion of CO_2 to methane by nickel nanoparticles supported on barium titanate. Adv Func Mater 2021; 31: 2008244, doi: 10.1002/adfm.202008244.

[26] Domen K., Kudo A., Onishi T. Mechanism of photocatalytic decomposition of water into H_2 and O_2 over $NiO_x/SrTiO_3$. J Catal 1986; 102: 92-98, doi: 10.1016/0021-9517(86)90143-0.

[27] Cui E., Lu G. Enhanced surface electron transfer by fabricating a core/shell Ni@NiO cluster on TiO_2 and its role on high efficient hydrogen generation under visible light irradiation. Int J Hydrog Energy 2014; 39: 8959-8968, doi: 10.1016/j.ijhydene.2014.03.258.

[28] Townsend T. K., Browning N. D., Osterloh F. E. Overall photocatalytic water splitting with $NiO_x/SrTiO_3$ – a revised mechanism. Energy Environ Sci 2012; 5: 9543-9550, doi: 10.1039/C2EE22665K.

[29] Chen W.-T., Chan A., Sun-Waterhouse D., Moriga T., Idriss H., Waterhouse G. I. N. Ni/TiO_2: a promising low-cost photocatalytic system for solar H_2 production from ethanol-water mixtures. J Catal 2015; 326: 43-53, doi: 10.1016/j.jcat.2015.03.008.

[30] Okemoto A., Tanaka K., Kudo Y., Gohda S., Koshiba Y., Ishida K., et al. Hydrogen production for photocatalytic decomposition of water with urea as a reducing agent. Catal Today 2018; 307: 231-236, doi: 10.1016/j.cattod.2017.01.035.

[31] Indra A., Menezes P. W., Kailasam K., Hollmann D., Schröder M., Thomas A., et al. Nickel as a co-catalyst for photocatalytic hydrogen evolution on graphitic-carbon nitride (sg-CN): what is the nature of the active species? Chem Commun 2016; 52: 104-107, doi: 10.1039/C5CC07936E.

[32] Zhang L., Liu Q., Aoki T., Crozier P. A., Structural evolution during photocorrosion of Ni/NiO core/shell cocatalyst on TiO_2. J Phys Chem C 2015; 119: 7207-7214, doi: 10.1021/jp512907g.

[33] Liu X., Yang X., Cui J., Wu C., Sun Y., Du X., et al. Ni coated with N-doped graphene layer as active and stable H_2 evolution cocatalysts for photocatalytic overall water splitting. ASC Catal 2023; 13: 14314-14223, doi: 10.1021/acscatal.3c0405.

[34] Liu R., Yoshida H., Fujita S.-I., Arai M. Photocatalytic hydrogen production from glycerol and water with NiO_x/TiO_2 catalysts. Appl Catal B: Environ 2014; 144: 41-45, doi: 10.1016/j.apcatb.2013.06.024.

[35] Fujita S.-I., Kawamori H., Honda D., Yoshida H., Arai M. Photocatalytic hydrogen production from aqueous glycerol solution using NiO/TiO_2 catalysts: effects of preparation and reaction conditions. Appl Catal B: Environ 2016; 181: 818-824, doi: 10.1016/j.apcatb.2015.08.048.

[36] Liu J., Li Y., Ke J., Wang S., Xiao H. Black $NiO\text{-}TiO_2$ nanorods for solar photocatalysis: recognition of electronic structure and reaction mechanism. Appl Catal B: Environ 2018; 224: 705-714, doi: 10.1016/j.apcatb.2017.11.028.

[37] Lin Z., Du C., Yan B., Wang C., Yang G. Two-dimensional amorphous NiO as a plasmonic photocatalyst for solar H_2 evolution. Nat Commun 2018; 9: 4036, doi: 10.1038/s41467-018-06456-y.

[38] Han K., Haiber D. M., Knöppel J., Lievens C., Cherevko S., Crozier P. et al. CrO_x-mediated performance enhancement of $Ni/NiO\text{-}Mg:SrTiO_3$ in photocatalytic water splitting. ACS Catal 2021; 11: 11049-11058, doi: 10.1021/acscatal.1c03104.

[39] Song R., Luo B., Geng J., Song D., Jing D. Photothermocatalytic hydrogen evolution over Ni_2P/TiO_2 for full-spectrum solar energy conversion. Ind Eng Chem Res 2018; 57: 7846-7854, doi: 10.1021/acs.iecr.8b00369.

[40] Chen Y., Qin Z. General applicability of nanocrystalline Ni_2P as a noble-metal-free cocatalyst to boost photocatalytic hydrogen generation. Catal Sci Technol 2016; 6: 8212-8221, doi: 10.1039/c6cy01653g.

[41] Fang S., Hu Y. H. Thermo-photo catalysis: a whole greater than the sum of its parts. Chem Soc Rev 2022; 47: 8203-8237, doi: 10.1039/d1cs00782c.

[42] Li W., Elzatahry A., Aldhayan D., Zhao D. Core-shell structured titanium dioxide nanomaterials for solar energy utilization. Chem Soc Rev 2018; 47: 8203-8237, doi: 10.1039/c8cs00443a.

[43] Talebi P., Singh H., Rani E., Huttula M., Cao W. Surface plasmon-driven photocatalytic activity of $Ni@NiO/NiCO_3$ core-shell nanostructures. RSC Adv 2021; 11: 2733-2743, doi: 10.1039/d0ra09666k.

[44] Talebi P., Kistanov A. A., Rani E., Singh H., Pankratov V., Pankratova V., King G., Huttula M., Cao W. Unveiling the role of carbonate in nickel-based plasmonic core@shell hybrid nanostructure for photocatalytic water splitting. Appl Energy 2022; 322: 119461, doi: 10.1016/j.apenergy.2022.119461.

[45] Perkins J. Shape memory effects in alloys. Plenum Press, New York 1975.

[46] Duerig T., Pelton A., Stockel D. An overview of nitinol medical applications. Mater Sci Eng 1999; A 273: 149-160, doi: 10.1016/S0921-5093(99)00294-4.

[47] O. Godard, M. Lagoudas, D. Lagoudas, Design of Space Systems Using Shape Memory Alloys, In Proc. of SPIE, Smart Structures and Materials, San Diego, CA 5056, USA 2003; 545-558, doi: 10.1117/12.483469.

[48] Nikitenko S. I., Chave T., Cau C., Brau H.-P., Flaud V. Photothermal hydrogen production using noble-metal-free $Ti@TiO_2$ core-shell nanoparticles under visible-NIR light irradiation. ACS Catal 2015; 5: 4790-4795, doi: 10.1021/acscatal.5b01401.

[49] Nikitenko S. I., Chave T., Le Goff X. Insights into the photothermal hydrogen production from glycerol aqueous solutions over noble metal-free Ti@TiO_2 core-shell nanoparticles. Part Part Syst Charact 2018; 35: 1800265, doi: 10.1002/ppsc.201800265.

[50] Castro A. T., Cuéllar E. L., Méndez U. O., Yacamán M. J. Advances in developing TiNi nanoparticles. Mater Sci Eng 2006; A 438-440: 411-413, doi: 10.1016/j.msea.2006.02.157.

[51] Huang X., Ackland G. J., Rabe K. M. Crystal structures and shape-memory behavior of NiTi. Nat Mater 2003: 2; 307-311, doi: 10.1038/nmat884.

[52] Tian H., Schryvers D., Liu D., Jiang Q., Humbeeck J. V. Stability of Ni in nitinol oxide surfaces. Acta Biomater 2011; 7: 892-899, doi: 10.1016/j.actbio.2010.09.009.

[53] Firstov G. S., Vitchev R. G., Kumar H., Blanpain B., Van Humbeeck J. Surface oxidation of NiTi shape memory alloy. Biomaterials 2012; 23: 4863-4871, doi: 10.1016/s0142-9612(02)00244-2.

[54] Ren H., Yang J.-L., Yang W.-M., Zhong H.-L., Lin J.-S., Radjenovic P. M., et al. Core-shell-satellite plasmonic photocatalyst for broad-spectrum photocatalytic water splitting, ACS Materials Lett 2021; 3: 69-76, doi: 10.1021/acsmaterialslett.0c00479.

[55] Wagner C. D., Naumkin A., Kraut-Vass A., Allison J. W., Powell C. J., Rumble J. R. NIST standard reference database 20, version 4.1. 2003, doi: 10.18434/T4T88K.

[56] Grosvenor A. P., Biesinger M. C., Smart R. St. C., McIntyre N. S. New interpretations of XPS spectra of nickel metal and oxides. Surf Sci 2006; 600: 1771-1779, doi: 10.1016/j.susc.2006.01.041.

[57] Peeters J. M., van Faassen E. E. H., Bakker C. J. G. Magnetic resonance imaging of phase transitions in nitinol. J Biomed Mater Res A 2007; 80A: 938–945, doi: 10.1002/jbm.a.30966.

[58] He X., Shi H. Size and shape effects on magnetic properties of Ni nanoparticles. Particuology 2012; 10: 497-502, doi: 10.1016/j.partic.2011.11.011.

[59] He X., Zhong W., Au C.-T., Du Y. Size dependence of the magnetic properties of Ni nanoparticles prepared by thermal decomposition method. Nanoscale Res Lett 2013; 8: 446, doi: 10.1186/1556-276X-8-446.

[60] Kreibig U., Vollmer M. Optical properties of metal clusters. Springer, New York, USA 1994.

[61] Pirzadeh Z., Pakizeh T., Miljkovic V., Langhammer C., Dmitriev A. Plasmon-interband coupling in nickel nanoantennas. ACS Photonics 2014; 1: 158-162, doi: 10.1021/ph4000339.

[62] Zubritskaya I., Lodewijks K., Maccaferri N., Mekonnen A., Dumas R. K., Akerman J., Vavassori P., Dmitriev A., Active magnetoplasmonic ruler. Nano Lett 2015; 15: 3204-3211, doi: 10.1021/acs.nanolett.5b00372.

[63] Govorov A. O., Richardson H. H. Generating heat with metal nanoparticles. Nano Today 2007; 2: 30-38, doi: 10.1016/S1748-0132(07)70017-8.

[64] Fang S., Sun Z., Hu Y. H. Insights into the thermos-photo catalytic production of hydrogen from water on a low-cost NiO_x-loaded TiO_2 catalyst. ACS Catal 2019; 9: 5047-5056, doi: 10.1021/acscatal.9b01110.

[65] Iervolino G., Vaiano V., Murcia J. J., Lara A. E., Hernández J. S., Rojas H., et al. Photocatalytic production of hydrogen and methane from glycerol reforming over Pt/TiO_2-Nb_2O_5. Int J Hydrog Energy 2021; 46: 38678-38691, doi: 10.1016/j.ijhydene.2021.09.111.

[66] Davda R. R., Shabaker J. W., Huber G. W., Cortright R. D., Dumesic J. A. A review of catalytic issues and process conditions for renewable hydrogen and alkanes by aqueous-phase reforming of oxygenated hydrocarbons over supported metal catalysts. Appl Catal B: Environ 2005; 56: 171-186, doi: 10.1016/j.apcatb.2004.04.027.

[67] Imai H., Yamawaki M., Li X. Direct synthesis of methane from glycerol by using silica-modified nickel catalyst. J Japan Petr Inst 2017; 60: 311-321, doi: 10.1627/jpi.60.311.

[68] Kandiel T. A., Ivanova I., Bahnemann D. W. Long-term investigation of the photocatalytic hydrogen production on platinized TiO_2: an isotopic study. Energy Environ Sci 2014; 7: 1420-1425, doi: 10.1039/C3EE41511B.

[69] Yu S., Jain P. K. Isotope effects in plasmonic photosynthesis. Angew Chem Int Ed 2020; 59: 22480-22483, doi: 10.1002/anie.202011805.

[70] El Hakim S., Chave T., Nikitenko S. I. Deciphering the reaction mechanisms of photothermal hydrogen production using H/D kinetic isotope effects. Catal Sci Technol 2022; 12: 5252-5256, doi: 10.1039/D2CY01185A.

[71] Kakiuchi M. Distribution of isotopic water molecules, H_2O, HDO, and D_2O, in vapor and liquid phases in pure water and aqueous solution systems. Geochim Cosmochim. Acta 2000; 64: 1485-1492, doi: 10.1016/S0016-7037(99)00281-1.

[72] Meng X., Wang T., Liu L., Ouyang S., Li P., Hu H., et al. Photothermal conversion of CO_2 into CH_4 with H_2 over group VIII nanocatalysts: an alternative approach for solar fuel production. Angew Chem Int Ed 2014; 53: 11478-11482, doi: 10.1002/ange.201404953.

[73] Sastre F., Puga A. V., Liu L., Corma A., Garcia H. Complete photocatalytic reduction of CO_2 to methane by H_2 under solar light irradiation. J Am Chem Soc 2014; 136: 6798-6801, doi: 10.1021/ja500924t.